

Multipath Measurements at the Lunar South Pole from Opportunistic Ground-based Observations — Part II: Experiment Results

Nereida Rodriguez-Alvarez,* Marc Sanchez Net,* Daniel Kahan,* David D. Morabito,* and Harvey M. Elliott†

ABSTRACT. — This article describes experimental results of the measurement campaign to quantify multipath fading effects between the Lunar Reconnaissance Orbiter (LRO) and the Deep Space Network (DSN) when the spacecraft sets behind or rises from the back-side of the Moon. This article presents, therefore, experimental scientific results involving multi-path fading and terrain characterization at the lunar south pole, while a companion paper provides a description of the experiment concept. All experiments were conducted opportunistically, meaning that they did not impose any operational constraints or requirements on LRO. Consequently, the approach expedited the measurement campaign, but also limited the resulting science output. In this report, we discuss the results from the bistatic radar measurements regarding the scattering area estimation and the signatures of lunar surface roughness observed on the Doppler Spread (DS) and the Circular Polarization Ratio (CPR). These measurements provide opportunistic information that has the potential to be used to better understand the Moon's surface roughness at scales of ~ 13.2 cm for future human exploration missions.

I. Introduction

This article is the second part of a companion article discussing an opportunistic bistatic experiment at the lunar poles [1]. As described in Part I, the performed experiment is based on LRO's S-band (2271.2 MHz) downlink signal grazing the lunar surface as the spacecraft sets or rises from the far side of the Moon. Similar experiments have been carried out on the Moon, Venus, Mars, and Titan [2].

Bistatic radar is described as actively probing planetary surfaces using oblique reflection and scattering of microwave signals. Such observations provide statistical information on the root-mean-square (RMS) surface slopes, and on the regolith dielectric constant and

* Communications Architectures and Research Section.

† Flight Communications Systems Section.

density, at scales comparable to the radio wavelength. At S-band, this translates to tens of centimeters.

To conduct the experiment, a radio signal transmitted from LRO is scattered by the lunar surface, and the echo is received at a DSN ground station on Earth. A direct signal from LRO is also received at the same time, providing a frequency reference for the echo. Due to the geometry constraints of the opportunistic experiment, measurements are obtained only at grazing angles, i.e., at incidence angles $\theta \approx 90^\circ$. Consequently, the bistatic angle for the LRO–Moon–DSN geometry of the received signal is $\varphi \approx 180^\circ$. Several tracks were performed during the project (see Table 1). More information on their timing and how they were set up can be found in [1].

Table 1. List of tracks showing date and sampled area on the surface of the Moon.

Track Identifier	Date	Sampled Area on the Moon
48161	DoY 65 at 05:33 UTC, 2020	Nobile Crater
48162	DoY 65 at 07:30 UTC, 2020	Nobile Crater
48247	DoY 72 at 05:48 UTC, 2020	Ashbrook Crater
48248	DoY 72 at 07:45 UTC, 2020	Ashbrook Crater
48249	DoY 72 at 09:42 UTC, 2020	Ashbrook Crater
48261	DoY 73 at 07:51 UTC, 2020	North Pole
48274	DoY 74 at 10:31 UTC, 2020	North Pole
48592	DoY 100 at 06:11 UTC, 2020	North Pole
48810	DoY 118 at 01:13 UTC, 2020	Spudis Ridge

DoY – Day of Year

The data employed in this study was recorded at 100 kbps with 16-bit resolution using an Open Loop Receiver (OLR) connected to a DSN station. Raw data samples outputted from the OLR are in the form of in-phase (I) and quadrature (Q) components. These were post-processed to obtain the power spectral density (PSD) of the received signal.

Figure 1 plots one such PSD and highlights how the differential Doppler shift between the direct and reflected paths (yellow line vs. light blue markings) separate the received echo

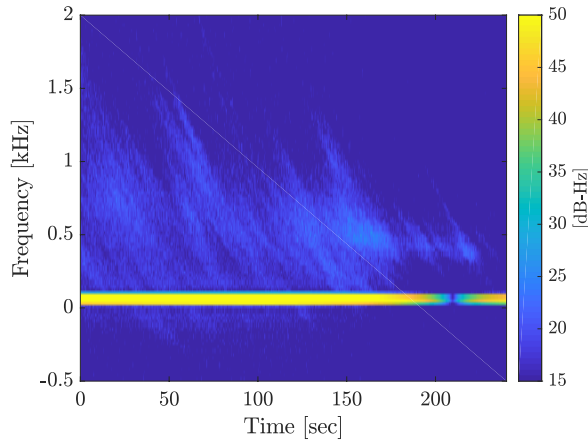


Figure 1. Example of PSD image for Track 48247.

from the carrier. In other words, the Doppler effects observed on the direct signal will be different from the Doppler effects observed on the reflected echo as the latter interacts with the Moon's surface topography. Therefore, the dispersion of the echo itself, measured from the obtained PSDs in the form of a Doppler Spread (DS), provides a measure of the RMS slope of those surface features [3], i.e. the surface roughness.

The Circular Polarization Ratio (CPR) is another parameter that is known to describe the surface's topographical features [4]. An incident signal transmitted at Right Circular Polarized (RCP) will generate a reflected signal with both the original RCP polarization and orthogonal Left Circular Polarized (LCP) polarization. Therefore, the CPR is computed as the ratio of power received in the RCP and LCP polarizations. However, this observable was only computed as a function of time for track 48810, since RCP and LCP measurements were not available for any of the other tracks.

Given that both the DS and the CPR have been shown to correlate to topological features such as surface roughness, we compare values derived from our opportunistic bistatic radar experiment with data collected from alternative space-based instruments, most notably the Lunar Orbiter Laser Altimeter (LOLA) onboard LRO. Centimeter-scale vertical resolution information is already available from LOLA. However, since those measurements are provided as point measurements, applying spatial interpolation to analyze bigger spatial areas will degrade the resolution. Prior to this comparison, however, we first detail our methodology to calculate the scattering area, and then provide an exploratory analysis of the collected observables.

A. Experiment Limitations

The experiments we conducted had several limitations:

1. In normal bistatic experiments, Fresnel reflection theory can be used to calculate the dielectric constant of the terrain being mapped once the direct and reflected echoes in each polarization have been calibrated. This measured dielectric constant can be related to porosity, through a model, and then to material density. However, in order to properly measure reflectivity and dielectric constant, the bistatic radar experiment need to be performed near the Brewster angle. As previously mentioned, the current experiment observes the LRO downlink signal after reflection from the Moon's surface at grazing angles ($\theta \approx 90^\circ$) that are away from the Brewster angle. Indeed, the lunar surface is expected to have a dielectric constant on the order 1.5 to 3.0, which results in a Brewster angle of $\theta \approx 50^\circ$ – 60° . Therefore, our collected measurements cannot be used to directly estimate the terrain dielectric constant.
2. Since the transmitted signal by LRO is only a carrier, our experiment does not have time resolution information. Therefore, delay-Doppler information is not available and the definition of the scattering area becomes more challenging. To overcome this limitation, we define the methodology used to identify the scattering area using only the spectrogram of the received echo in Section II of this report.

II. Scattering Area Estimation

The size of the scattering area contributing to the total power in the bistatic radar configuration depends on various parameters: the transmitting antenna, the receiving antenna, whether the geometry is favorable, and the characteristics of the surface. In the case of this experiment, we dealt with two potential limiting factors: 1) the projection of the LRO transmitting antenna, which pointed towards Earth but still illuminated the Moon surface at grazing angles ($\theta \approx 90^\circ$); and 2) the diffuse scattering originating from terrain areas away from the specular point (due to the surface roughness properties).

In normal bistatic radar experiments, when delay-Doppler images are obtained, the power measured with different delay and Doppler frequencies can be mapped into iso-range and iso-Doppler lines on the surface of the Moon. For instance, Figure 2 shows a bistatic radar configuration in which a Global Navigation Satellite System (GNSS) satellite is the source of transmission. The signal is reflected from the surface of the Earth in the form of forward scattering and the resulting signal is measured by a receiver located in a different spacecraft.

Figure 2 also shows how the scattering area is characterized using a grid of iso-delay and iso-Doppler lines. Although there is a certain level of uncertainty in the measurement because most delay-Doppler values can be mapped to two points on the surface (see magenta circles), the maximum measured delay and Doppler values provide a method for estimating the extent of the scattering area. Indeed, they can be translated into the contour of an ellipse (iso-range line) and two hyperbolas (iso-Doppler line) that, together, clearly delimit the region over which scattering has occurred. This methodology has been used in [6] for Earth applications.

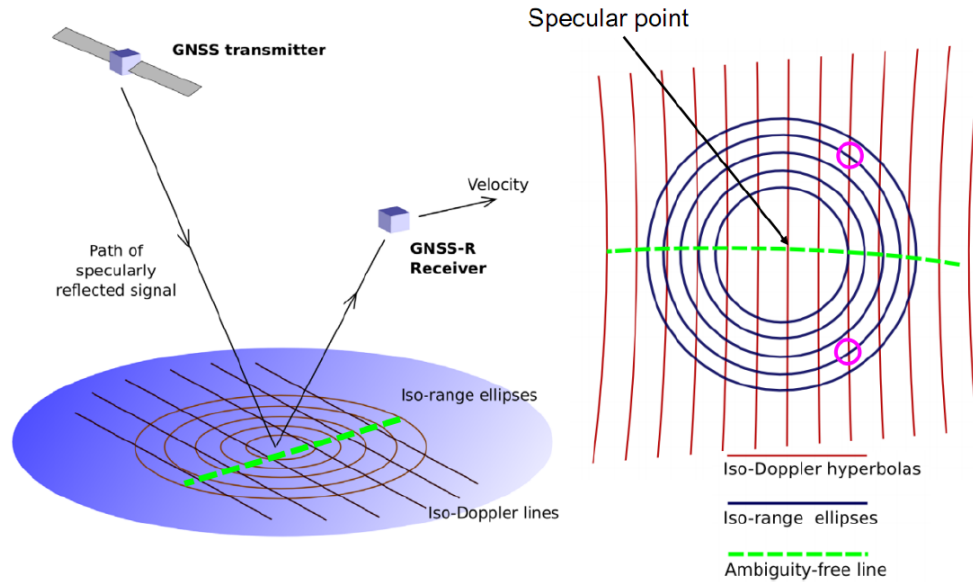


Figure 2. Iso-Doppler and iso-range lines (image credit: Reference [5])

A. General Definition of the Scattering Area

Due to the opportunistic nature of our experiment, the signal transmitted by LRO only provided us with information on the Doppler shift experienced by the reflection (i.e., our measurements had no delay information). Therefore, we could not use the previously described method. Instead, we relied on the concept of the Fresnel zone number as a proxy to the iso-range lines. In other words, we first assumed the scattering area to be elliptical in shape, and then calculated its extent by estimating the number of Fresnel zones that should be included in the scattering area so that the resulting ellipse has at least one point with the maximum measured Doppler shift. We henceforth assume that this methodology has been used to estimate the scattering area of all our experiments.

Given this general definition of the scattering area, two more factors need to be considered when estimating the final area that is contributing to the total power:

- **Surface roughness role:** If the surface of the Moon was perfectly smooth, then the scattering area would be close to that of the first Fresnel zone. However, as roughness increases, the scattering area is known to also increase and generally extends beyond the first Fresnel zone. An example of this phenomenon can be observed in bistatic radar experiments on Earth using the Global Positioning System (GPS) spacecraft as transmitter (L-band), and 600 km altitude satellites as receivers (e.g., Cyclone Global Navigation Satellite System – CYGNSS [7] or TechDemoSat-1 – TDS-1 [8]). In these experiments, both the transmit and receive antennas have large footprints on the Earth surface, so roughness is known to be the driving factor when calculating the scattering area. Indeed, when conducted over the ocean, bistatic experiments have scattering areas of 500 km in diameter, mostly due to the roughness induced by ocean waves. Alternatively, when the same experiment is conducted over a smooth lake, the scattering area is around 1 km to 3 km in diameter.
- **Antenna gain role:** If the antenna footprint on the ground is narrow, it can act as a filter that limits the measurable scattering area. This circumstance can be observed, for instance, in experiments conducted with Deep Space Station-13 (DSS-13) and LRO's mini-radio frequency (RF) instrument [9]. In this configuration, the transmitting antenna (DSS-13) is located at the DSN on Earth and pointed towards the spacecraft, while the receiving antenna on board LRO is pointed towards the Moon. Then, the directivity of the LRO antenna actively filters the size of the scattering area from where the signal is scattered. Similarly, a bistatic radar experiment conducted on Venus [10], by the Venus Express (VEX) spacecraft, also had the antenna footprint as its limiting factor, which was also pointed at the surface of the planet.

To understand whether our experiment is limited by surface roughness or the radiation pattern of the transmit/receive antennas, we have computed the size of the Fresnel zones as in [11], [12]. In particular the scattering area is assumed to be an ellipse of semi-major axis a and semi-minor axis b , which can be estimated using Equation (1) and Equation (2), respectively:

$$a = \frac{1}{\cos(\theta)} \sqrt{n\lambda \frac{R_{tx_s} R_{rx_s}}{R_{tx_s} + R_{rx_s}}} \quad (1)$$

$$b = \sqrt{n\lambda \frac{R_{tx_s}R_{rx_s}}{R_{tx_s}+R_{rx_s}}} \quad (2)$$

where:

- R_{tx_s} is the distance between transmitter and specular point.
- R_{rx_s} is the distance between receiver and specular point.
- n is the number of Fresnel zones.
- λ is the wavelength of the transmitted signal.
- θ is the incidence angle of the bistatic radar observation.

The extent of the Doppler shift experienced by the reflections from the lunar surface can be obtained from our measurements and, as previously mentioned, provides an indirect method to limit the number of Fresnel zones that must be included in the scattering area. In other words, to determine the scattering area, we progressively increase n in Equation (1) and Equation (2) until the Doppler shift experienced by any point inside of the ellipse corresponds to the maximum Doppler shift measured in the corresponding PSD (i.e., our general definition of the scattering area). As an example, Figure 3 provides an illustration of the intersection of the Doppler information and the ellipses computed from the Fresnel zone approximation.

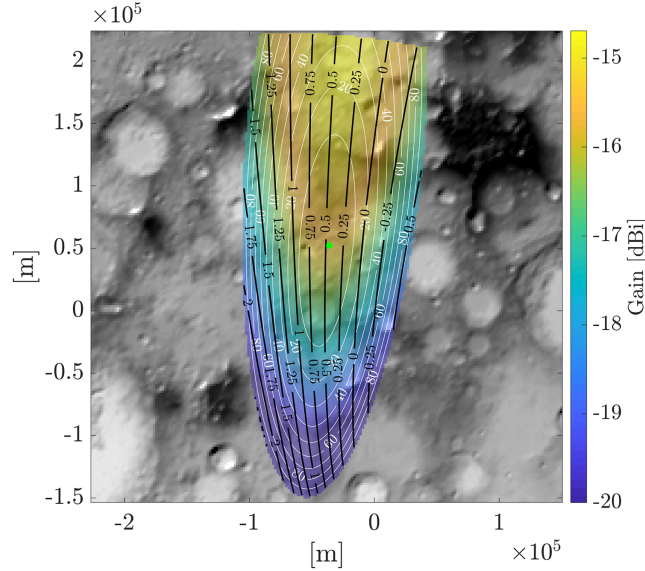


Figure 3. Example of the iso-Doppler lines and the iso-range lines (approximated to Fresnel zones)–computations for Track 48247, at time = 100 s from start. The data bar displays the antenna gain in dBi.

B. Role of Antenna Pattern and Surface Roughness on the Scattering Area

At this point we need to understand what is the limiting factor for our experiments, the antenna gain pattern or the roughness. Therefore, we can foresee three scenarios:

1. Scattering area limited by the roughness alone.

2. Scattering area limited by the antenna gain pattern alone.
3. A combination of both, roughness and gain pattern.

Note that in Figure 3, LRO's antenna radiation pattern is also plotted and the scattering area is represented by antenna gain values above -6 dB. Since the definition of the scattering zone is key to understanding the characteristics of the received signal after reflection on the Moon surface, we now provide for track 48161 a quick data analysis. In order to do that, we provide calculations of the mean roughness—obtained from LRO altimeter LOLA—and described in more detail in Section IV, averaged over different scattering areas as a function of time (Examples 1 to 3 below).

Example 1: Mean LRO's LOLA roughness value computed within the LRO full antenna footprint (larger than the one in Figure 3).

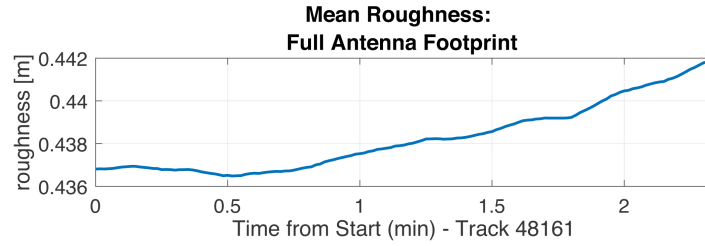


Figure 4. Example of the mean roughness observed within the LRO full antenna footprint—computations for Track 48161.

When considering the antenna footprint as the limiting factor (Figure 4), the surface roughness variations are smoothed out, yielding a total roughness variability over time of 6 mm, with a mean of 40 cm. This happens because the big footprint minimizes the mean roughness change between one instant of time and the next one, i.e., there is little change between one “snapshot” and the next. This method does not match the Doppler spread observed in the reflected signals, and thus will not be used in this article.

Example 2: Mean LRO Altimeter roughness value computed considering specular reflection (first Fresnel zone).

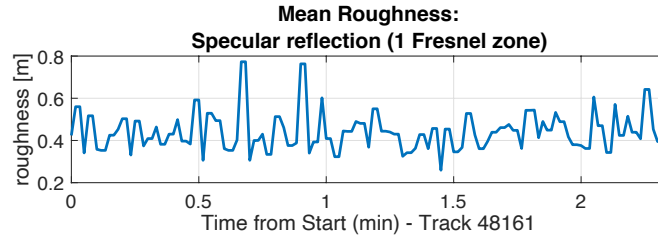


Figure 5. Example of the roughness observed at the specular point (first Fresnel zone)—computations for Track 48161.

When taking the roughness value at the most specular location (Figure 5), the observed surface roughness variability is larger, because the specular point from one “snapshot” to

the next has moved and therefore both measurements are uncorrelated. This results in a total roughness variability over time of 50 cm, with a mean of 42 cm. Unfortunately, in our experiment assuming a perfectly specular reflection is not valid since the Moon's surface is not smooth. Therefore, we do not use the first Fresnel zone to determine the scattering area in our calculations.

Example 3: Mean LRO altimeter roughness value computed considering general definition of the scattering area (Figure 3).

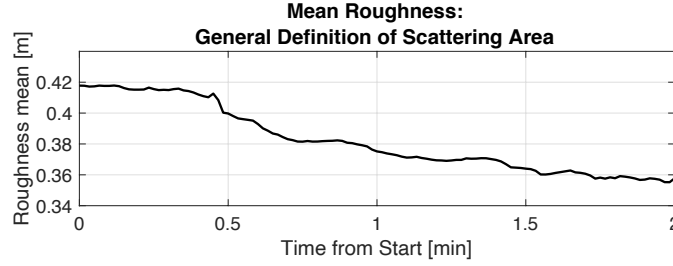


Figure 6. Example of the mean roughness observed within scattering area using our general definition—computations for Track 48161.

Because the values in Figure 6 are based on the direct measurements from our experiment and correctly capture the signal spread in the Doppler domain, we will assume our general definition of the scattering area as the right definition for our experiments. This leads to an observed total roughness variability over time in this case of 6 cm, with a mean of 38.5 cm. We recognize, however, that this method only approximates the delay spread of the scattered signal. This could potentially be smaller than the one defined by the iso-delay lines in Figure 3 due to filtering from the antenna footprint on the lunar surface. The main reason for this is the considerable footprint size resulting from pointing the antenna in such a way that the scattered signal is reflected at grazing angles.

III. Signatures of the Moon Roughness

In this section we investigate the signatures of the Moon's surface roughness from our available bistatic measurements. We describe two observables computed directly from the measurements: the *DS* and the *CPR*. In addition to those observables, we provide the reference mean surface roughness obtained from the LOLA instrument (described in Section IV) within the scattering area following the method described in Section II.A. After all the data are presented, we compare the reference roughness to the observables and comment on the impact of roughness variations in Section V.

A. Measurement Observable: Doppler Spread

The bistatic scattering process is characterized by many individual reflections originating from the multiple facets that are randomly located and specularly oriented on the Moon's surface. Each facet then produces a different frequency shift, i.e., each component represents the Doppler shift of the facets around the specular point. As previously mentioned, the rougher the surface, the wider the area on the surface contributing to the

total received power. Therefore, we conclude that the surface roughness must have a direct impact on the Doppler spread.

In this section, we focus on describing the variations observed primarily in the DS, since the surface roughness should be directly correlated with them. Figure 7 shows an example of the reflected signal.

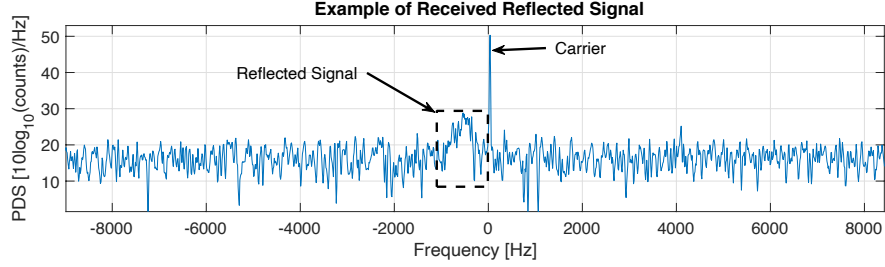


Figure 7. Example of received reflected signal during track 48161 at $t = 1 \text{ m } 40 \text{ s}$.

Figure 7 shows the PSD of the received signal at DSN station 1 minute and 60 seconds after starting track 48161. Close to the carrier, which propagates directly from the spacecraft, we note that the surface echo is clearly visible in the frequency domain, thus allowing us to directly estimate the DS. In particular, in order to compute its value, we have fit the power distribution of the reflected signal to a Gaussian kernel and then measured the bandwidth of the reflection by computing its 6σ width (i.e., the 99.9997% of the energy). Two examples of these computations are shown in Figure 8 and Figure 9.

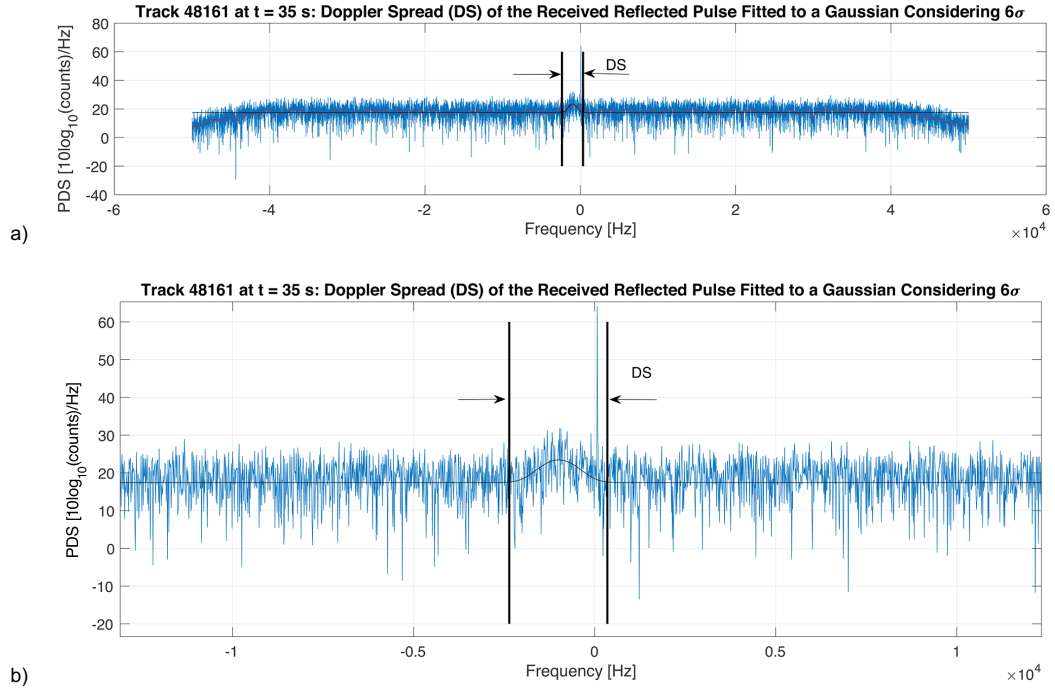


Figure 8. Example of DS calculation for the reflected signal during track 48161 at $t = 35 \text{ s}$: (a) full-frequency range, and (b) zoom into the region of interest.

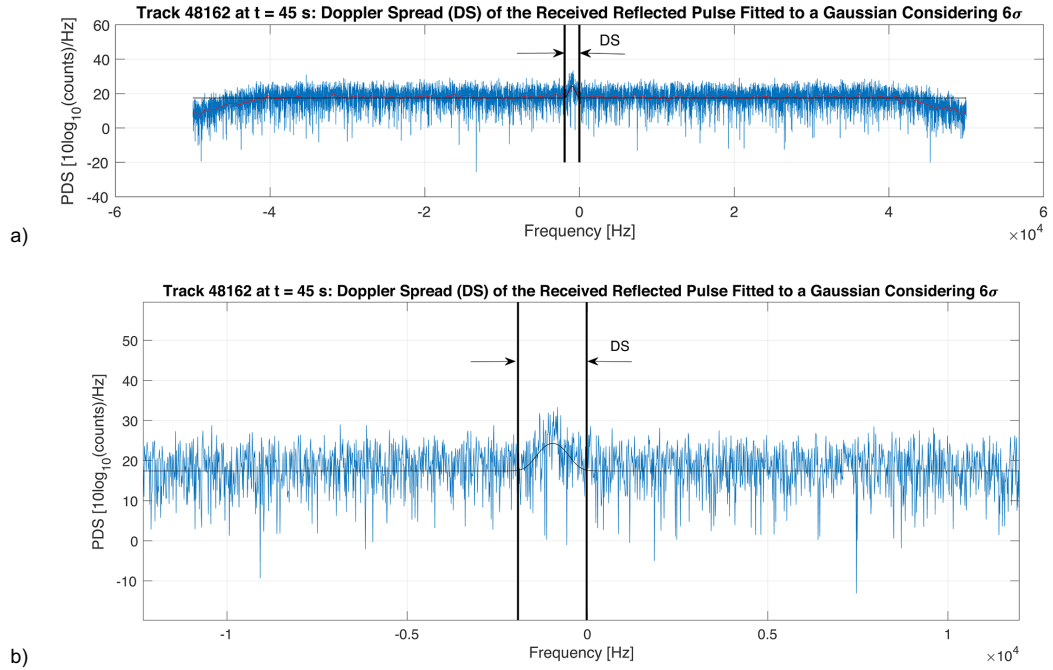


Figure 9. Example of DS calculation for the reflected signal during track 48162 at $t = 45$ s: (a) full-frequency range, and (b) zoom into the region of interest.

Observe that the 6σ criterion to define the DS provides a good representation of most of the received power from the echo. This 6σ algorithm for computing the DS has been applied to all available tracks. Figures 10 through 15 summarize the resulting DS estimates over time for all available tracks.

From these figures, one can observe the high correlation between the DS measurements obtained from track 48161 (Figure 10) and the DS measurements obtained from track 48162 (Figure 11). Those tracks correspond to observations very close in time for the same day of year and the same area, the Nobile crater. Tracks 48247 (Figure 12), 48248 (Figure 13), and 48249 (Figure 14) also show high correlation on the measured DS, and correspond to same day observations over the Ashbrook Crater. Alternatively, tracks 48261 (Figure 15), 48274 (Figure 16), 48592 (Figure 17), and 48810 (Figure 18) do not exhibit comparable trends since they correspond to three different areas: an area in close proximity to the north pole, a flat area, and an area north of the Spudis Ridge. Tracks 48261 (Figure 15) and 48592 (Figure 17) both correspond to an area in close proximity to the north pole but those measurements were taken 27 days apart, so the exact covered areas were far apart enough that the DS signature no longer matches.

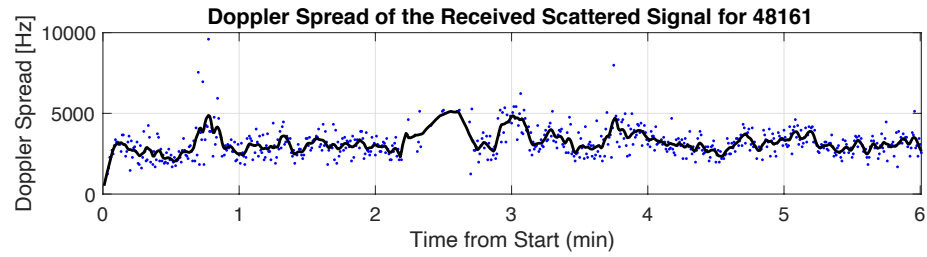


Figure 10. Doppler spread of the received scattered signal for track 48161. Measurements correspond to Nobile crater area on DoY 65, year 2020.

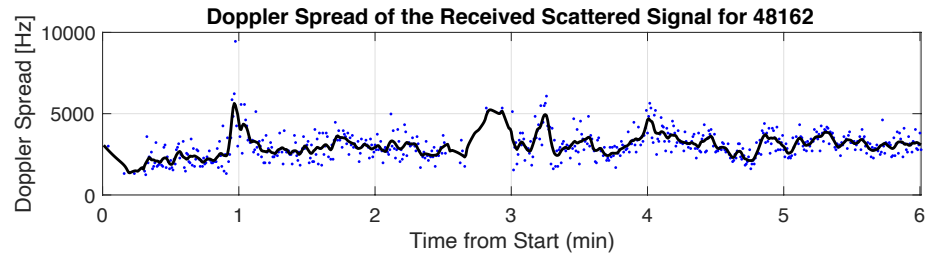


Figure 11. Doppler spread of the received scattered signal for track 48162. Measurements correspond to Nobile crater area on DoY 65, year 2020.

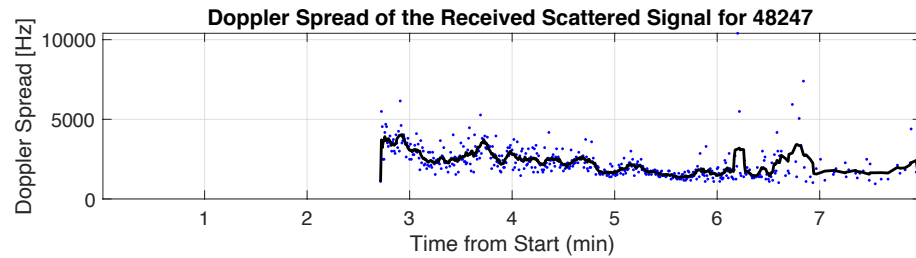


Figure 12. Doppler spread of the received scattered signal for track 48247. Measurements correspond to Ashbrook crater area on DoY 72, year 2020.

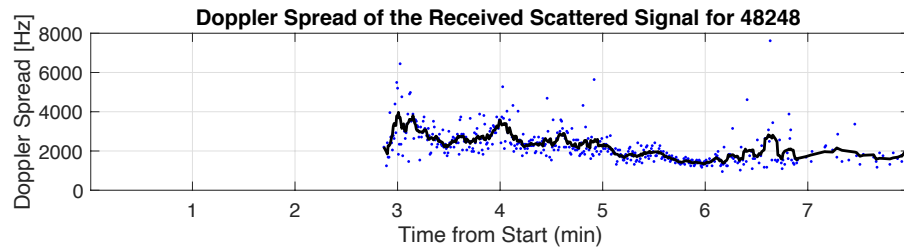


Figure 13. Doppler spread of the received scattered signal for track 48248. Measurements correspond to Ashbrook crater area on DoY 72, year 2020.

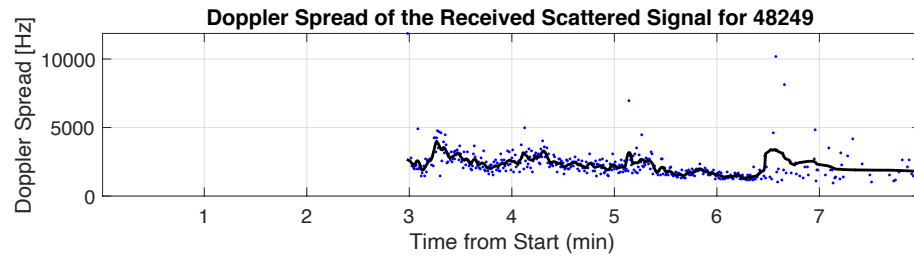


Figure 14. Doppler spread of the received scattered signal for track 48249. Measurements correspond to Ashbrook crater area on DoY 72, year 2020.

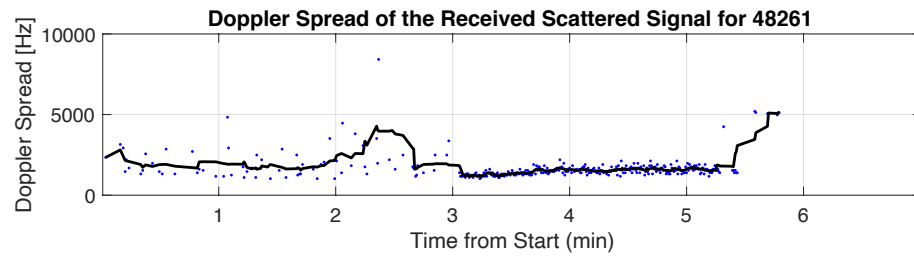


Figure 15. Doppler spread of the received scattered signal for track 48261. Measurements correspond to North Pole area on DoY 73, year 2020.

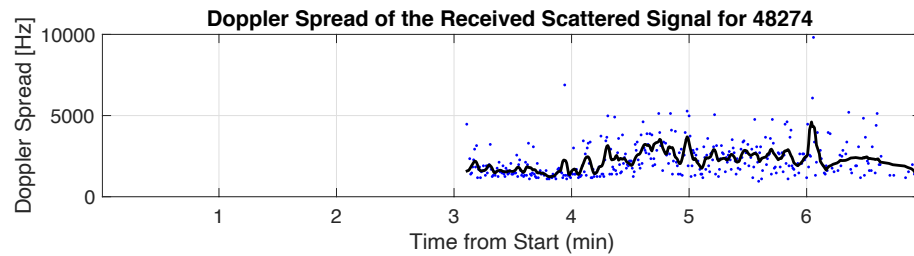


Figure 16. Doppler spread of the received scattered signal for track 48274. Measurements correspond to a flat area on DoY 74, year 2020.

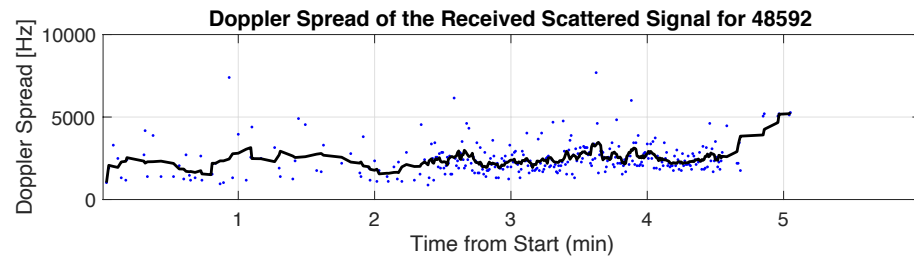


Figure 17. Doppler spread of the received scattered signal for track 48592. Measurements correspond to North Pole area on DoY 100, year 2020.

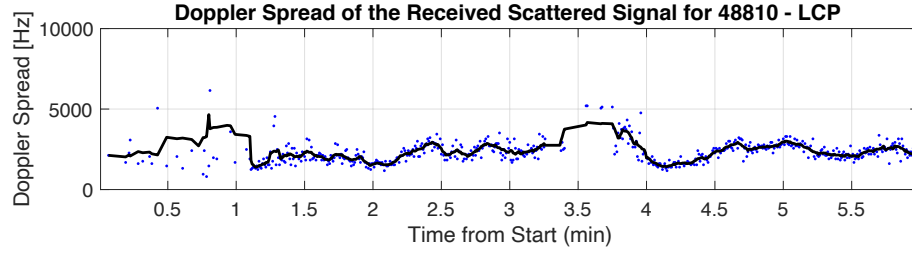


Figure 18. Doppler spread of the received scattered signal for track 48810. Measurements correspond to north Spudis Ridge area on DoY 118, year 2020.

Figure 19 shows the DS correlation between two tracks close in time and covering the same area (e.g., 48161 and 48162), and the correlation between tracks covering areas far apart (e.g., 48261 and 48592).

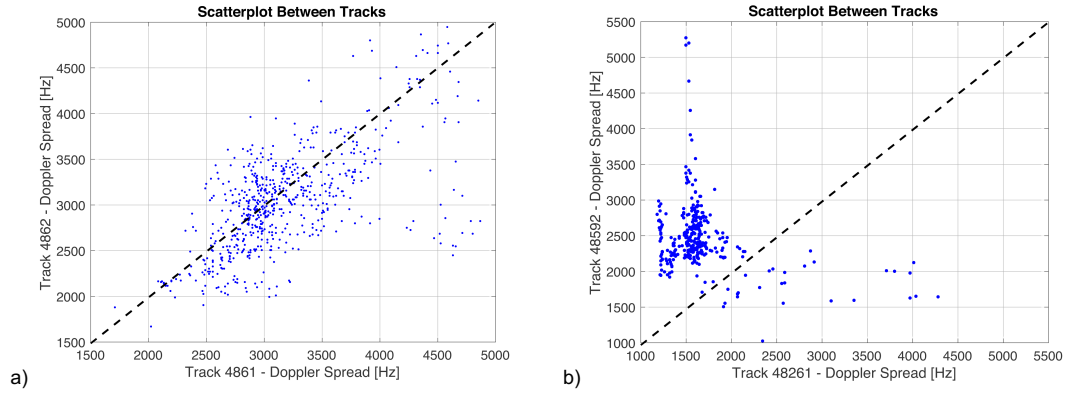


Figure 19. Correlation between tracks: (a) tracks close in time and covering the same area, i.e., 48161 and 48162, and (b) tracks covering close areas far apart on time, i.e., 48261 and 48592.

As it can be observed, Figure 18a shows a high degree of correlation ($\sim 70\%$), while Figure 18b shows no correlation between measurements. This clearly indicates that the measured Doppler spread is correlated with the physical properties of the surface being sampled during the bistatic radar experiment. This result, already noted in other works by Patterson (e.g., [9]) for small bistatic angles, has now also been confirmed when operating at grazing angles.

B. Measurement Observable: Circular Polarization Ratio

Previous studies have employed CPR as a descriptor of surface roughness—e.g., see [9] and [13]. Surfaces that are smooth at the scale of the wavelength will have a low CPR, i.e., the signal in the opposite sense will be stronger than the signal in the same sense. If the surface is rougher, then the polarization of the scattered wave will have an increased chance of changing twice, thus returning to the polarization state that was originally transmitted. Therefore, in this case, the amount of signal power received in the same sense polarization increases, making the CPR also increase in value.

In the case of our experiment, since LRO is transmitting RCP, the same sense and opposite sense polarizations are RCP and LCP, respectively. Figure 20 shows the total integrated

power for track 48810 and computed from the scattered signal measured in the same sense and opposite sense polarizations.

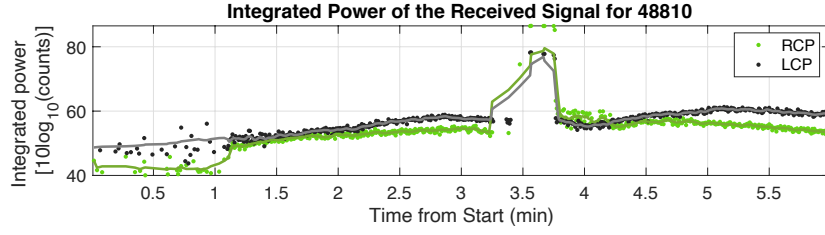


Figure 20. Integrated power of the received scattered signal for track 48810 at polarization RCP and LCP. Measurements correspond to north Spudis Ridge area on DoY 118, year 2020.

Based on these values, the measurement observable CPR simply is computed as in Equation 3:

$$CPR = \frac{I_{RCP}}{I_{LCP}} \quad (3)$$

where I_{RCP} is the integrated power at the RCP and I_{LCP} is the integrated power at the LCP within the reflected signal bandwidth. Note that to calculate the CPR we have only used the received power within the 6σ Doppler spread presented in the previous section. Therefore, we have excluded all power contributions from the direct line-of-sight signal.

Figure 21 shows the result for the CPR computation. As previously stated, the CPR lies closer to 1 when both RCP and LCP measurements are similar (indicative of rough surface), and it decreases as RCP measurements become weaker (indicative of smoother surfaces). In other words, a flat surface would show a CPR near 0, while a very rough surface would show a CPR near 1, always relative to the measurement wavelength.

Note that our CPR measurements show a strange behavior at times ranging from 3.25 min to 4.25 min from the beginning of the track, approximately. Since the cause for these sudden jumps in CPR ratio is not well understood, we have excluded this data from any further consideration in our analysis.

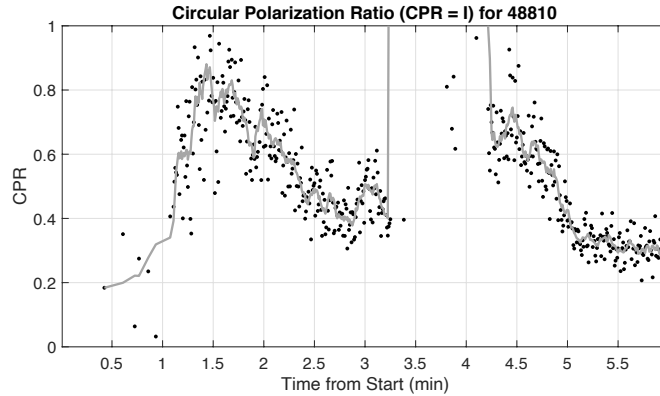


Figure 21. CPR computed for track 48810 from measurements at RCP and LCP polarizations. Measurements correspond to north Spudis Ridge area on DoY 118, year 2020.

IV. Reference Dataset: Roughness Information

The LOLA instrument onboard LRO has provided us with global topography maps of the lunar surface at high resolution, including altitude and roughness maps. Altitude maps are derived from the data collected from LOLA by computing the round-trip time of emitted laser pulses by the LOLA instrument, between the instant at which they are transmitted and the instant at which they are received. The round-trip time is an indirect measure of how far LRO is from the lunar surface which, when combined with knowledge of the LRO trajectory, translates into digital elevation maps of the lunar terrain. The lunar surface roughness, on the other hand, can be derived from the data collected from LOLA by analyzing the spread of the laser pulses after they are reflected from the Moon's surface. Figure 22 shows two different methods for estimating the Moon's roughness.

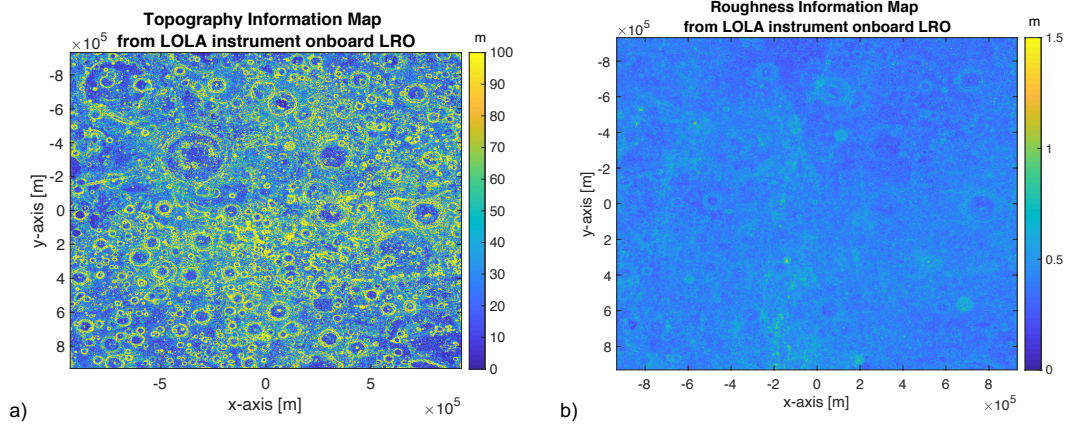


Figure 22. Moon surface topographic information maps obtained from LOLA instrument measurements onboard LRO: (a) ΔH , and (b) RMS of the surface heights (i.e., roughness).

The values on the maps are computed as the residual from three successive laser shots with $n - 3$ degrees of freedom after fitting a plane to $n = 5$ to 15 profile returns [14]. Depending on orbital velocity, probability of detection, and spacecraft altitude, the slope baseline may vary from 30 to 120 meters [14]. In the Figure 22a map, each pixel value represents the maximum surface height difference (ΔH) within slope baseline, while in the Figure 22b map, each value represents the RMS of the surface height differences within the slope baseline. In an attempt to obtain reference roughness information, we will use both maps as the representation of the roughness.

Assuming LOLA's datasets provide a roughness reference for our experiments, we have computed from those maps the averaged mean and standard deviation as descriptors of the topographic features observed by the LRO-DSN bistatic radar configuration at each instant of time within the scattering area (defined as Figure 3). The following plots show both the mean (ρ) and the standard deviation or coarseness (C) of the surface roughness features ΔH and RMS for the three more relevant tracks: track 48161, track 48247, and track 48810.

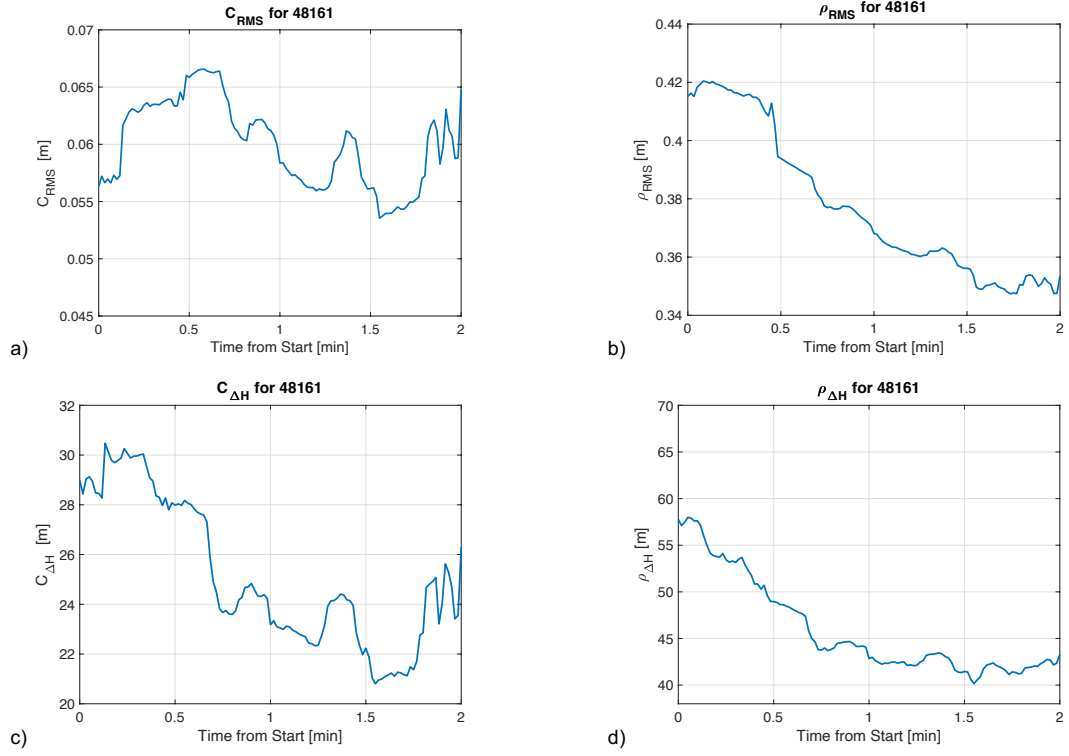


Figure 23. Track 48161 lunar surface information obtained from LOLA instrument onboard LR0:
(a) C_{RMS} , (b) ρ_{RMS} , (c) $C_{\Delta H}$, and (d) $\rho_{\Delta H}$.

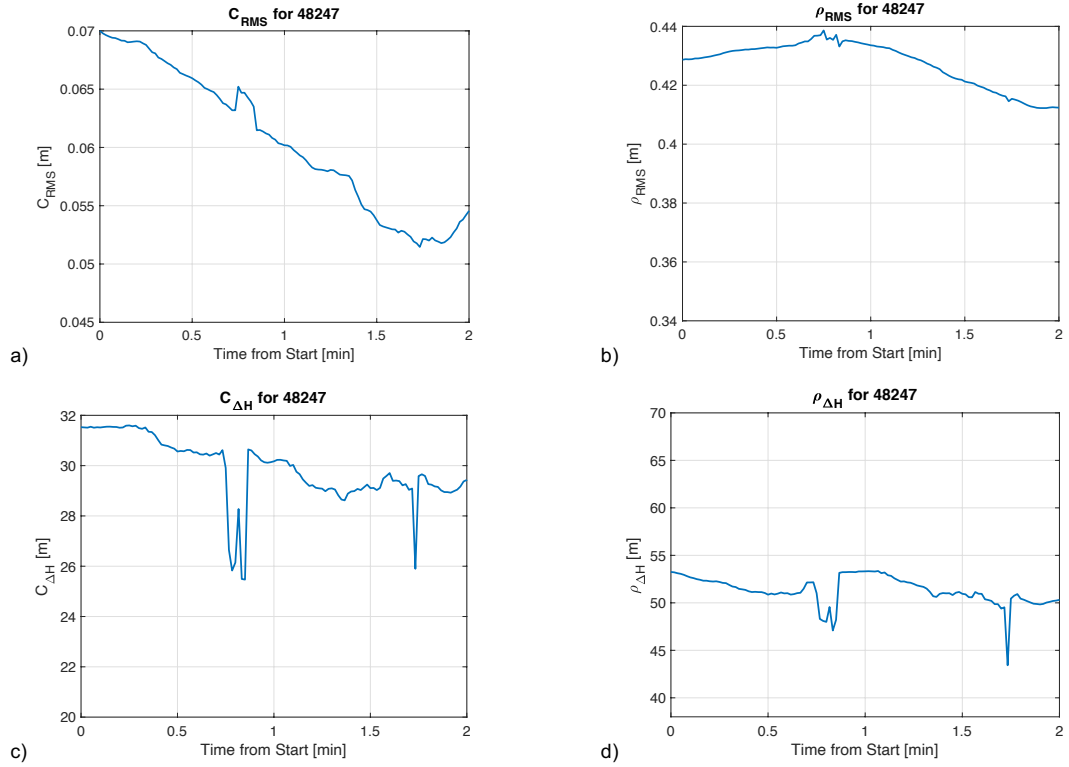


Figure 24. Track 48247 lunar surface information obtained from LOLA instrument onboard LR0:
(a) C_{RMS} , (b) ρ_{RMS} , (c) $C_{\Delta H}$, and (d) $\rho_{\Delta H}$.

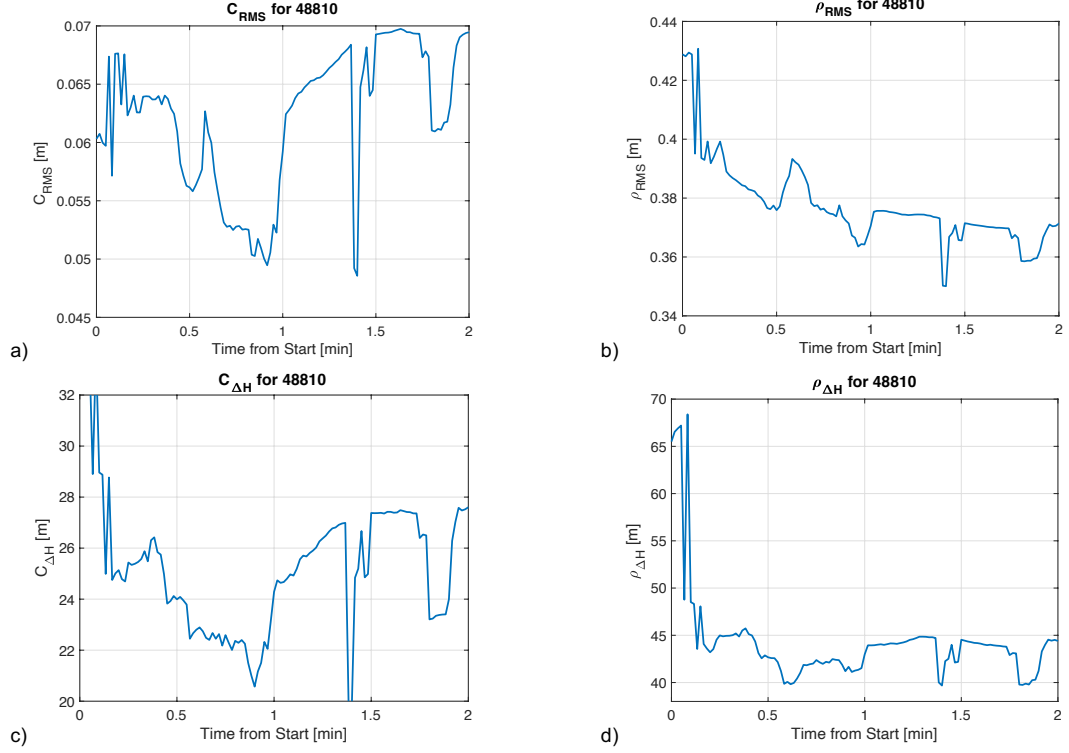


Figure 25. Track 48810 lunar surface information obtained from LOLA instrument onboard LRO:
(a) C_{RMS} , (b) ρ_{RMS} , (c) $C_{\Delta H}$, and (d) $\rho_{\Delta H}$.

We do not expect to get good agreement between our data and the LOLA reference dataset because the measurements obtained in this study are sensitive to roughness scales on the order of the transmitted signal wavelength (~ 13.2 cm), which differs from the assessments made by LOLA, i.e., a multi-beam laser altimeter that operates at a wavelength of 1064.4 nm. Simply by inspecting Figure 23 to Figure 25, we can automatically discard $C_{\Delta H}$, and $\rho_{\Delta H}$ as valid references for the lunar surface roughness, since the observable shows variations >20 meters in all tracks. Even though it is an accepted definition of roughness, it does not capture the variation scales that our measurements are sensitive to. The standard definition of roughness is indeed in terms of RMS. Given all the limitations of the reference dataset towards our measurements, we perform the comparisons with respect to C_{RMS} and ρ_{RMS} in next section.

V. Experiment Results

This section compares the DS and CPR observables to the reference roughness estimates obtained from the LOLA altimeter data as shown in Figure 23, Figure 24, and Figure 25. We only consider C_{RMS} and ρ_{RMS} . Our roughness estimates correspond to an area of the surface based on the iso-lines filter adjusted from the Doppler spread computed at each single measurement.

It has been demonstrated in [15] that the Doppler spread is nearly proportional to the tangent of the surface roughness parameter, more specifically the unidirectional RMS slope:

$$\tan(\beta) = \frac{DS}{4(2\ln 2)^{0.5} v_s \cos(\gamma_s)} \quad (4)$$

where:

- $\tan(\beta)$ is the unidirectional RMS slope
- DS is the Doppler spread of the reflected pulse
- v_s is the velocity of the specular point on the surface
- γ_s is the incidence angle of the bistatic configuration at the specular point.

Note that the specular point velocity v_s and the incidence angle of the bistatic configuration γ_s variables in Equation 4 are obtained from the metadata associated with each track, i.e., position information of both DSN and LRO over time.

In order to perform the comparisons for the DS measurement observable and the reference topographic descriptors, we have first transformed the DS into $\tan(\beta)$. Therefore, $\tan(\beta)$ is a sub-product of the main observable, computed following Equation 4, which according to [14], is the parameter sensitive to the surface roughness. Next we show the results for three selected tracks in Figures 26, 27, and 28, comparing the variations between $\tan(\beta)$ and the corresponding lunar roughness descriptors: mean (ρ) and standard deviation or coarseness (C) of the RMS roughness.

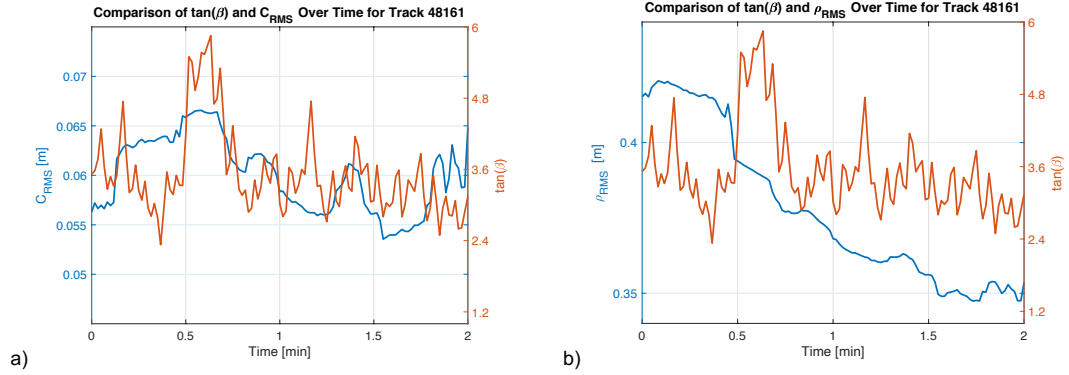


Figure 26. Track 48161. Comparison between $\tan(\beta)$ and the four lunar surface descriptors computed from LOLA onboard LRO: (a) C_{RMS} , and (b) ρ_{RMS} .

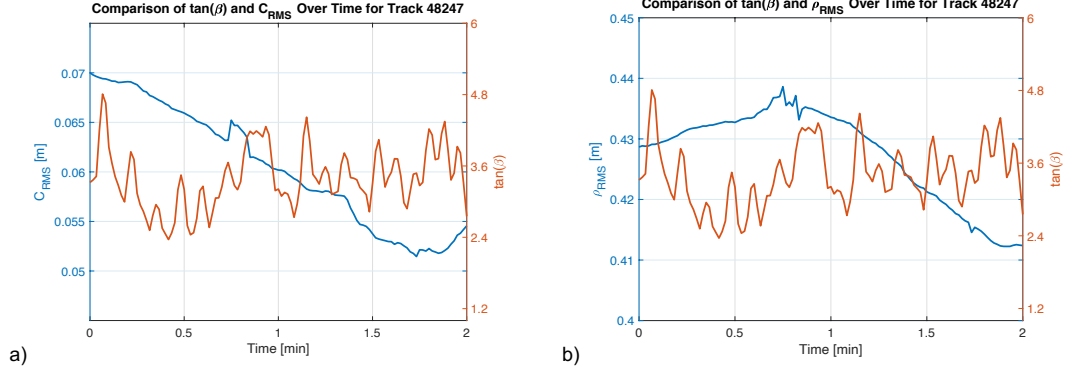


Figure 27. Track 48247. Comparison between $\tan(\beta)$ and the four lunar surface descriptors computed from LOLA onboard LRO: (a) C_{RMS} , and (b) ρ_{RMS} .

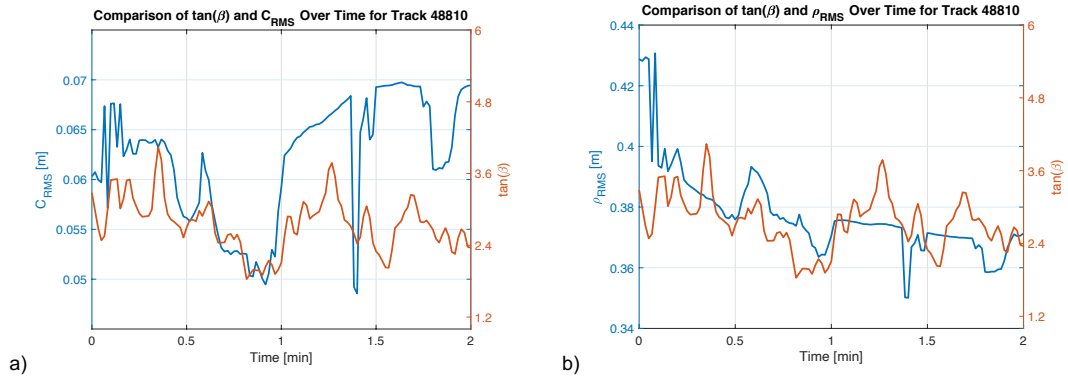


Figure 28. Track 48810. Comparison between $\tan(\beta)$ and the four lunar surface descriptors computed from LOLA onboard LRO: (a) C_{RMS} , and (b) ρ_{RMS} .

Upon inspection of the variations observed in the different tracks, we see that the $\tan(\beta)$ presents a pattern showing more oscillations than the reference roughness maps derived from the LOLA instrument. At this point, it is important to remember that the DS parameter is expected to describe variations at the scale of the wavelength of the transmitted signal (~ 13.2 cm) and therefore the echo is responding to a different scale of the topographical features than those described by the LOLA's altimeter measurements.

Results for track 48161 and track 48810 are more consistent with the topographic descriptors than those for track 48247. In particular, these results show weak correlations with the C_{RMS} computed within the scattering area, than for ρ_{RMS} . Track 48810 shows better agreement with all topographic descriptors than the data of the other two tracks, but the rationale for this agreement remains unexplained.

Next, we present the comparison for the CPR measurement observable and the lunar surface information obtained from the LOLA instrument onboard LRO for track 48810, the only track with two simultaneous polarization measurements. Figure 29 summarizes these results.

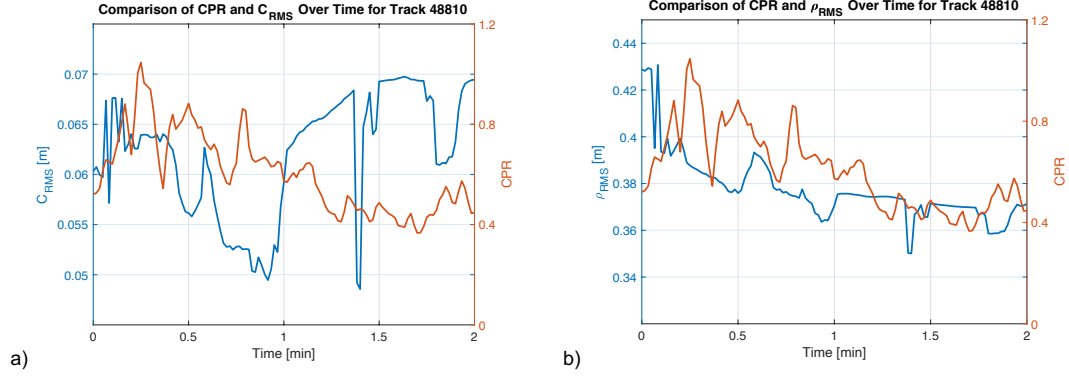


Figure 29. Track 48810. Comparison between CPR and the four lunar surface descriptors computed from LOLA onboard LRO: (a) C_{RMS} , and (b) ρ_{RMS} .

The results obtained comparing CPR to the topographic descriptors differ from the $\tan(\beta)$ analysis, which showed better agreement for the C_{RMS} descriptor. In this case the most significant agreement is obtained from the comparison between CPR and ρ_{RMS} . However, the overall level of correlation is, as previously noted for the case of $\tan(\beta)$, quite weak.

VI. Conclusions

We have performed an analysis of the lunar south pole soil roughness properties based on measurements from an opportunistic bistatic radar experiment between LRO and the DSN at grazing angles. We have employed two observables, the Doppler spread and the Cross Polarization Ratio, and have studied the variability of those observables compared to various descriptors of the lunar surface topographic features. The lunar surface topographic maps have been obtained from LRO's LOLA altimeter data, which have been averaged within the approximate scattering area of the received signal. This scattering area has been found empirically using the observed Doppler spread in the measurements together with the Fresnel number method.

The main results of this article show that there is a certain degree of agreement between the observables, DS and CPR, and the RMS surface topographic descriptor. Given a larger measurement dataset and a more suitable reference dataset, the CPR and/or DS can be placed into an algorithm to produce a lunar surface roughness map. This opportunistic information has the potential to be used to better understand the Moon's surface roughness at scales of ~ 13 cm for future human exploration missions.

Keeping in mind that the measurements are mostly sensitive to surface roughness features on the order of the transmitted signal wavelength (13.2 cm), and that the LOLA's altimeter reference dataset provides RMS roughness values on the order of 40 cm in mean, there is an intrinsic error associated to the comparisons of both datasets. In other words, the reference roughness maps from LRO lack spatial resolution to be directly comparable with our observables, which were measured at S-band. A better reference dataset would have been results from an independent study where S-band is used to assess surface roughness, or even roughness measurements from other studies at X-band, as the ones developed under

the DSS-13/mini-RF project [9], whose wavelength is about one-fourth of the wavelength in our experiments, and therefore results are comparable.

Future research should incorporate more suitable data for validating our techniques. For example, a collaboration with the project led by W. Patterson will be very beneficial since the mini-RF S-band polar mosaics can be used to validate our CPR data. Also, a collaboration with the LRO Diviner team would significantly improve our results by incorporating surface rock abundance maps for rocks in the cm-size range. This work from the LRO Diviner team was led by Catherine Elder, at the Jet Propulsion Laboratory (JPL), and the maps produced, although not yet publicly available, will be key to better understand our measurements.

Acknowledgments

We would like to thank Jack Lippincott of the Deep Space Network, Ralph Casasanta of LRO Ground System and Operations Support, George Martinez of JPL (Network Operations Project Engineer), Steve Slojkowski (Flight Dynamics Facility Lead) of Omitron, Goddard Space Flight Center (GSFC), Rick Saylor of National Aeronautics and Space Administration (NASA) GSFC, and Harvey W. Elliott of NASA GSFC, for their help and contributions while planning and executing this project.

We would also like to thank the external reviewer, Wes Patterson, for all his comments and suggestions, and for taking the time to look into this document and evaluate our work.

References

- [1] M. Sanchez Net, N. Rodriguez-Alvarez, D. Kahan, D. Morabito, H.M. Elliot, “Multipath Measurements at the Lunar South Pole from Opportunistic Ground-based Observations — Part I: Experiment Concept,” *The Interplanetary Network Progress Report*, vol. 42-221, Jet Propulsion Laboratory, Pasadena, CA, pp. 1–30, 15 August 2020. [https://ipnpr.jpl.nasa.gov/progress report/ 42-221/42-221C.pdf](https://ipnpr.jpl.nasa.gov/progress%20report/42-221/42-221C.pdf)
- [2] R. Simpson, “Planetary exploration,” pp. 56–77, 2007. [https://digital-library.theiet.org/ content/books/10.1049/sbra001e ch5](https://digital-library.theiet.org/content/books/10.1049/sbra001e_ch5)
- [3] S. Asmar, R. French, E. A. Marouf, et al., “Cassini radio science user’s guide,” Report for Jet Propulsion Laboratory, Pasadena, California, 2018.
- [4] B. A. Campbell, High circular polarization ratios in radar scattering from geologic targets, *J. Geophys. Res.*, vol. 117, E06008, 2012. [doi:10.1029/2012JE004061](https://doi.org/10.1029/2012JE004061).
- [5] D. Yang, “Soil Moisture Content Detection based on GNSS Reflected Signal and its Applications.” Electronic Presentation.
- [6] N. Rodriguez-Alvarez, S. Misra, E. Podest, M. Morris, X. Bosch-Lluis, The Use of SMAP-Reflectometry in Science Applications: Calibration and Capabilities. *Remote Sens.*, vol. 11, p. 2442, 2019.

- [7] C. Ruf, M. Unwin, J. Dickinson, R. Rose, D. Rose, M. Vincent, and A. Lyons, "Cygness: Enabling the future of hurricane prediction [remote sensing satellites]," *IEEE Geoscience and Remote Sensing Magazine*, vol. 1, no. 2, pp. 52–67, 2013.
- [8] M. Unwin, P. Jales, J. Tye, C. Gommenginger, G. Foti, and J. Rosello, "Spaceborne gnss- reflectometry on techdemosat-1: Early mission operations and exploitation," *IEEE Journal of Selected Topics in Applied Earth Observations and Remote Sensing*, vol. 9, no. 10, pp. 4525–4539, 2016.
- [9] W. Patterson, A. Stickle, F. Turner, J. Jensen, D. Bussey, P. Spudis, R. Espiritu, R. Schulze, D. Yocky, D. Wahl, et al., "Bistatic radar observations of the Moon using mini-RF on LRO and the Arecibo Observatory," *Icarus*, vol. 283, pp. 2–19, 2017.
- [10] R. A. Simpson, G. L. Tyler, B. Häusler, R. Mattei, and M. Pätzold, "Venus express bistatic radar: High-elevation anomalous reflectivity," *Journal of Geophysical Research: Planets*, vol. 114, no. E9, 2009.
<https://agupubs.onlinelibrary.wiley.com/doi/abs/10.1029/2008JE003156>
- [11] P. Beckmann and A. E. Spizzichino, *The Scattering of Electromagnetic Waves from Rough Surfaces*. Norwood, MA: Artech House, 1987, reprint. Originally published: Oxford; New York: Pergamon Press, 1963. (International series of monographs on electromagnetic waves, v. 4).
- [12] A. Ghasemi, A. Abedi, and F. Ghasemi, *Propagation Engineering in Wireless Communications*. New York: Springer, 2011.
- [13] A. Virkki, K. Muinonen, and A. Penttilä, "Inferring asteroid surface properties from radar albedos and circular-polarization ratios," *Meteoritics & Planetary Science*, vol. 49, no. 1, pp. 86–94, 2014. <https://onlinelibrary.wiley.com/doi/abs/10.1111/maps.12161>
- [14] LOLA gridded data record slope map (GDRDSM). Source of information available online at https://ode.rsl.wustl.edu/moon/pagehelp/quickstartguide/index.html?lola_gdrdsm.htm
- [15] G. L. Tyler and D. H. H. Ingalls, "Functional dependences of bistatic-radar frequency spectra and cross sections on surface scattering laws," *Journal of Geophysical Research (1896–1977)* vol. 76, no. 20, pp. 4775–4785, 1971.